ISSN 1063-7737, Astronomy Letters, 2010, Vol. 36, No. 1, pp. 44–58. © Pleiades Publishing, Inc., 2010.
Original Russian Text © S.V. Shestov, S.V. Kuzin, A.M. Urnov, A.S. Ul'yanov, S.A. Bogachev, 2010, published in Pis'ma v Astronomicheskiĭ Zhurnal, 2010, Vol. 36, No. 1, pp. 46–60.

Solar Plasma Temperature Diagnostics in Flares and Active Regions from Spectral Lines in the Range 280–330 Å in the SPIRIT/CORONAS-F Experiment

S. V. Shestov[1,2*], S. V. Kuzin[1], A. M. Urnov[1,2], A. S. Ul'yanov[1,2], and S. A. Bogachev[1]

[1] *Lebedev Physical Institute, Russian Academy of Sciences, Leninskii pr. 53, Moscow, 119991 Russia*
[2] *Moscow Physicotechnical Institute, Dolgoprudnyi, Moscow oblast, 141700 Russia*
Received May 4, 2009

Abstract—Plasma temperature diagnostics in solar flares and active regions has been carried out using data from the SPIRIT spectroheliograph onboard the CORONAS-F satellite. The temperature distribution of the differential emission measure (DEM) has been determined from the relative intensities of spectral lines recorded in the spectral range 280–330 Å in the period from 2001 to 2005. Analysis of these distributions has led to the conclusion about the existence of active regions with various "characteristic" temperature compositions. The presence of a hot plasma with temperatures $\log T = 6.8–7.2$ in active regions has been established for the first time from XUV spectroscopic data and monochromatic X-ray line images. The DEM distribution for intense long-decay flares has also been obtained for the first time and a similarity of the temperature compositions for flares of different classes at the decay phase has been found. The spectra have been modeled on the basis of the calculated DEMs. The systematic discrepancies between the calculated and measured line intensities are discussed.

DOI: 10.1134/S1063773710010056

Key words: *CORONAS-F, SPIRIT, XUV spectra, flares, active regions, differential emission measure.*

INTRODUCTION

The temperature, density, and emission measure (EM) are the most important parameters that characterize the state of astrophysical and laboratory plasmas. Obtaining experimental information about various distributions of these quantities, in particular, the temperature distribution for the EM is needed to construct theoretical models of stable plasma structures and activity phenomena in the solar corona—flares, active regions, coronal loops, etc. The most complete data on the physical conditions in the solar plasma can be obtained by the method of spectroscopic diagnostics based on an analysis of spectral images in short-wavelength spectral ranges. However, in the X-ray range this method was implemented only with broadband filters in the Yohkoh and Hinode experiments with a small number of spectral channels. Therefore, diagnostics based on spectral images containing a large number of XUV emission lines is a very topical task. Owing to the relatively low excitation thresholds of such lines compared to X-ray ones, the possible distortions introduced by nonthermal electrons with $E \gg kT$ do not affect the rate of their excitation and, thus, the electron distribution may be considered Maxwellian.

The XUV spectroscopic observations performed with the SERTS, SOHO/CDS, SUMER, and CORONAS-F/SPIRIT spectrographs for individual compact regions of the solar corona in the absence of flares suggest the simultaneous existence of a plasma with various temperatures, from $T \sim 80\,000$ K to $T \sim 5\,000\,000$ K (MK), for example, in active regions (Brosius et al. 1996; Landi and Landini 1998; Zhitnik et al. 2006), coronal loops (Landi and Feldman 2008; Schmelz et al. 2008), and streamers (Warren and Warshall 2002).

The question about the presence of a plasma with a high temperature, >5 MK, is very important for solving the problem of active-region heating. Although the "hot" Fe XVII (SERTS), Fe XVI, Si XII, Fe XXIII (CDS) and Ni XIX, Fe XIX (SUMER) lines fall within the spectral ranges of the above spectrographs, using them for plasma temperature diagnostics in practice encounters certain difficulties. This is because the intensities of these lines are determined with a low accuracy due to the low relative intensity in the investigated regions (Brosius et al. 2000; Landi and Landini 1998). Therefore, multiply

*E-mail: sshestov@dgap.mipt.ru

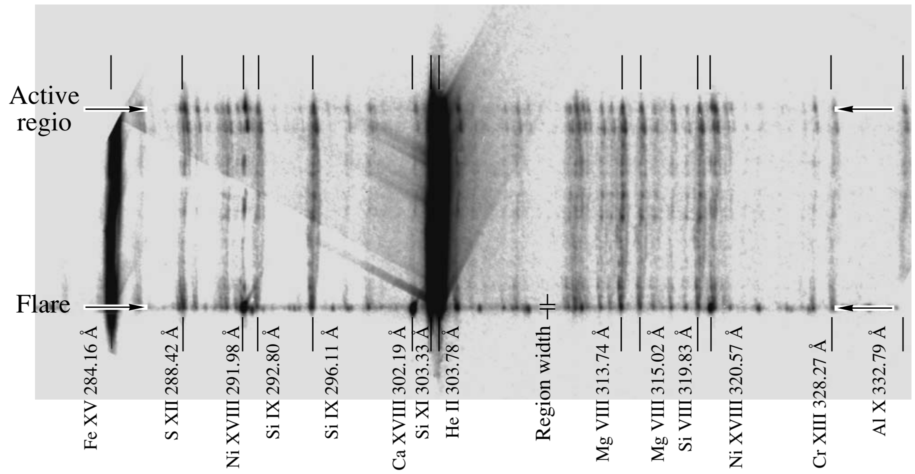

Fig. 1. Spectroheliogram taken in the range 280–330 Å at 21:21 UT on December 28, 2001. Some of the spectral images are labeled and the positions of the flare (X3.4 class, the maximum at 20:30) and the active region NOAA 9742 used here are marked; the size of the region over which the spectrum was taken is also marked.

repeated measurements of spectral lines formed in a wide temperature range, including those at "flare" temperatures ≥10 MK for a large number of plasma structures, are needed to obtain the most complete and accurate characteristic of the phenomena.

At present, investigating the hot plasma of flares is particularly topical, since the number of recorded XUV flare spectra is small and there are virtually no observations of strong flares. The difficulty of recording flares is related to their poor predictability, compact sizes, and short lifetimes. In the case of spectrographs with a limited field of view (as in the SERTS and CDS/SOHO experiments), the probability of recording a flare is low, because the entire Sun cannot be observed simultaneously. Thus far, the main source of information on spectral lines observed during a flare has been the catalog of spectral lines compiled from observations in the 1970s by the slitless spectroheliograph onboard the Skylab station (Dere 1978) based on an M2 flare.

These restrictions were partly overcome in the SPIRIT experiment (Zhitnik et al. 2002) onboard the CORONAS-F satellite (Oraevsky and Sobelman 2002). The SPIRIT instrumentation included two independent XUV spectroheliographs that recorded monochromatic images of the full solar disk in the spectral ranges 176–207 Å and 280–330 Å (see Beigman et al. 2005).

Systematic observations of the Sun by the SPIRIT instrumentation were performed from September 2001 to December 2005. Tens of thousands of spectroheliograms, including more than a hundred spectroheliograms containing solar flares, were taken. The spectra of very intense X-class solar flares at various phases of their development had been taken for the first time.

In this paper, we present the technique and results of plasma temperature diagnostics in solar flares and active regions based on an analysis of the differential emission measure (DEM). The DEM was determined from the relative intensities of spectral lines in the range 280–330 Å obtained from SPIRIT data. Our main objectives were to choose the spectral lines in the range 280–330 Å, to determine the DEM from SPIRIT/CORONAS-F data, to determine the DEM for the plasma of various phenomena and structures in the solar corona from spectroheliograph data, and to model the spectra in the range 280–330 Å to detect possible systematic deviations in the experimental and model spectra. In our calculations, we used the CHIANTI 5.2.1 software and data (Landi et al. 2006).

OBSERVATIONS

The XUV Spectroheliograph Onboard the CORONAS-F Satellite

Coronas-F (Oraevsky and Sobelman 2002), the second satellite of the Russian–Ukrainian program to investigate the solar activity, operated in orbit from mid-2001 to late 2005. There was the SPIRIT instrumentation (Zhitnik et al. 2002) designed at the Lebedev Physical Institute, Russian Academy of Sciences, onboard the satellite.

The SPIRIT instrumentation included XUV spectroheliographs for the spectral ranges 176–207 and 280–330 Å. The spectroheliographs were based on a slitless scheme with a planar grazing-incidence diffraction grating. The optical scheme and parameters of the XUV spectroheliographs are given in Beigman et al. (2005). When the slitless scheme is used, monochromatic images of the *full* solar disk are

Table 1. List of observed objects

№	Time, UT	Object	Note
1	06:38 Nov. 4, 2001	AR	NOAA 9684, SOT
2	21:21 Dec. 28, 2001	AR	NOAA 9742
3	00:34 Apr. 20, 2002	AR	NOAA 9906, SOT
4	19:24 Apr. 20, 2002	AR	»
5	20:32 Apr. 21, 2002	AR	»
6	18:41 Dec. 24, 2002	AR	NOAA 0223, 0225, 0229
7	09:06 Dec. 27, 2002	AR	NOAA 0223, 0225, 0229
8	03:21 Jan. 11, 2003	AR	NOAA 0254
9	04:06 Feb. 02, 2003	AR	NOAA 0276
10	16:48 Feb. 25, 2004	AR	NOAA 0564
11	17:02 Mar. 13, 2004	AR	–
12	17:07 July 25, 2004	AR	NOAA 0652 SOT
13	03:59 Sep. 16, 2001	F	M6.1 flare (max at ∼03:53)
14	05:21 Nov. 17, 2001	F	M2.8 flare (max at ∼05:20)
15	08:29 Nov. 17, 2001	F	M2.8 flare (»)
16	13:20 Sep. 11, 2005	F	M3.2 flare (max at 13:11), measured n_e^{**}
17	02:17 Sep. 16, 2005	F	M4.8 flare (max at 01:49) + M2.2(max at 02:20), measured n_e^{**}
18	21:21 Dec. 28, 2001	F	X3.4 flare (max at ∼20:30), published spectrum*, SOT
19	02:08 July 16, 2004	F	X1.4 flare (max at 02:06), measured n_e^{**}
20	03:29 July 16, 2004	F	X1.4 flare (»)
21	10:42 Jan. 17, 2005	F	X4.1 flare (max at ∼09:50), SOT
22	18:34 Sep. 7, 2005	F	X17 flare (max at 17:40)
23	20:04 Sep. 7, 2005	F	X17 flare (»), measured n_e^{**}
24	21:35 Sep. 7, 2005	F	X17 flare (»), measured n_e^{**}
25	21:48 Sep. 8, 2005	F	X5.5 flare (max at 21:06), measured n_e^{**}
26	23:19 Sep. 8, 2005	F	X5.5 flare (»), measured n_e^{**}
27	20:29 Sep. 9, 2005	F	X6.2 flare (max at 20:03), measured n_e^{**}
28	21:59 Sep. 9, 2005	F	X6.2 flare (»), measured n_e^{**}
29	22:12 Sep. 10, 2005	F	X2.2 flare (max at ∼22:05)
30	23:43 Sep. 10, 2005	F	X2.2 flare (»)
31	19:48 Sep. 13, 2005	F	X1.5 flare (max at 19:28), measured n_e^{**}
32	21:19 Sep. 13, 2005	F	X1.5 flare (max at 20:04), measured n_e^{**}

Note. AR is the active region, and F is the flare. The time is the initial spectroheliogram recording time. The simultaneously recorded active regions and flares were observed at different locations of the solar disk. For the flares, the X-ray class and time of flare maximum were taken from GOES data. The AR numbers are given according to the NOAA classification. *—the catalog of spectral lines was published in Beigman et al. (2005), **—the measured densities were published in Shestov et al. (2009). SOT—the event was chosen for investigation from the SOTERIA International Program, http://soteria-space.eu.

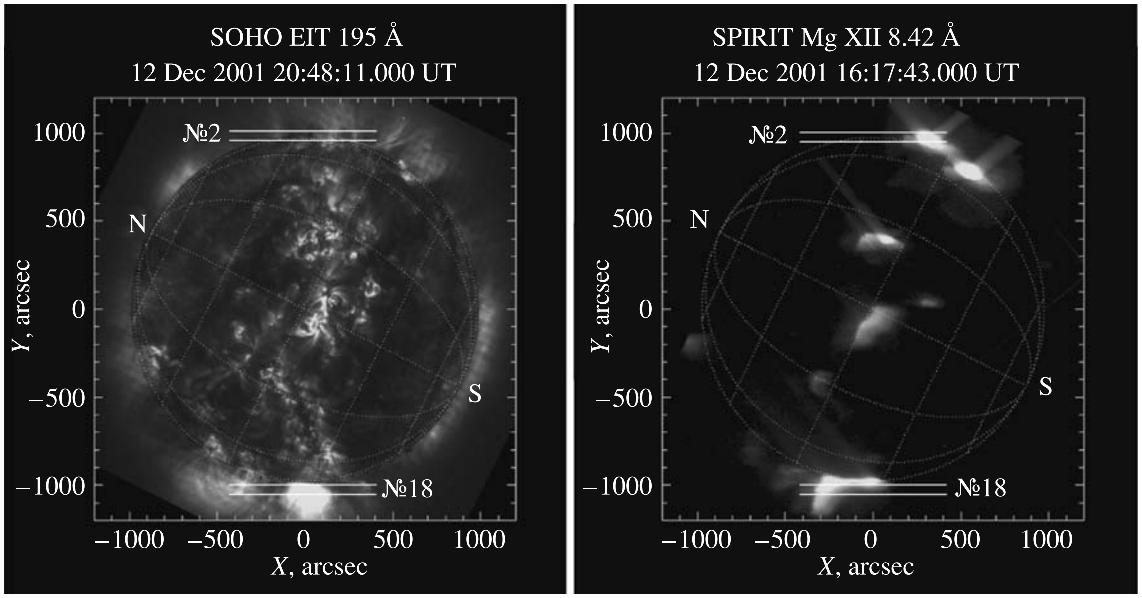

Fig. 2. Images of the solar corona obtained on December 28, 2001, by the EIT telescope onboard SOHO near 195 Å (a) and by the SPIRIT Mg XII spectroheliograph at $\lambda = 8.42$ Å (b). The areas for which the spectra were taken are marked: the active region NOAA 9742 (object no. 2) and the X3.4 flare (object no. 18), see Table 1.

formed on the spectroheliograph detector. The peculiarities of the scheme include the absence of emission in higher diffraction orders, while the small width of the solar image along the dispersion axis, 0.5 Å, reduces the overlap of the images in neighboring spectral lines. Using such an optical scheme in the SPIRIT XUV spectroheliographs allowed one to take more than 100 spectroheliograms containing solar flares, including more than ten spectroheliograms in the range 280–330 Å containing extremely intense X-class solar flares.

Observations with the SPIRIT XUV spectroheliographs were used to compile a catalog of spectral lines in the range 280–330 Å observed in an X3.4 flare (Beigman et al. 2005) and a catalog of spectral lines observed in an M5.6 flare (Shestov et al. 2008). The density of the plasma with a temperature of ∼1–3 MK in flares (including X-class ones), active regions, and quiet-Sun regions was determined from the relative intensities of Fe XI–Fe XIII spectral lines in the range 176–207 Å (Shestov et al. 2009).

In this paper, we used the XUV spectroheliograph data in the range 280–330 Å obtained from September 2001 to September 2005 to determine the DEM. The spectral line intensities were determined by taking into account an updated spectral sensitivity of the SPIRIT instrumentation. We used the spectroheliograms containing X- and M-class solar flares taken at different decay phases and the spectroheliograms taken in a flareless period.

Choosing the Objects

In this paper, we used the spectra of 32 observed objects for our analysis—long-decay solar flares and active regions. We used 15 spectra of X-class flares taken at different phases, 5 spectra of M-class flares, and 12 spectra of active regions. A full list of all the observations used, along with comments, is presented in Table 1. The table gives the class and time of maximum for the flares as measured by the GOES[1] X-ray monitors; the active region numbers are given according to the NOAA[2] (National Oceanic and Atmospheric Administration) classification.

An example of a spectroheliogram in the range 280–330 Å containing an X3.4 flare (object no. 18) and an active region (object no. 2) is shown in Fig. 1. The spectroheliogram was taken at 21:21 UT on December 28, 2001. Some of the spectral images are labeled, the positions of the flare and the active region used here are marked, and the size of the region over which the spectrum was taken is marked.

Figure 2 presents the solar-corona images recorded at close instants of time. Figure 2a presents the image in the spectral range near 195 Å obtained by the EIT telescope onboard SOHO; Fig. 2b presents the monochromatic image of the Sun in the Mg XII $\lambda = 8.42$ Å spectral line obtained by the SPIRIT

[1]http://www.ngdc.noaa.gov/stp/GOES/goes.html.
[2]see, e.g., http://www.solar.ifa.hawaii.edu/ARMaps/-archive.html.

Table 2. Spectral lines in the range 280–330 Å used to calculate the DEM

Ni XVIII	$\lambda = 291.98$ Å	$3p^2P_{3/2} \to 3s^2S_{1/2}$
Fe XXII	$\lambda = 292.46$ Å	$2s2p^2\,{}^4P_{3/2} \to 2s^22p^2P_{3/2}$
Si IX	$\lambda = 296.11$ Å	$2s2p^3\,{}^3P_2 \to 2s^22p^2\,{}^3P_2$
Ca XVIII	$\lambda = 302.19$ Å	$1s^22p^2P_{3/2} \to 1s^22s^2S_{1/2}$
Si XI	$\lambda = 303.33$ Å	$2s2p^1P_1 \to 2s^2\,{}^1S_0$
Fe XX	$\lambda = 309.29$ Å	$2s^22p^3\,{}^2P_{3/2} \to 2s^22p^3\,{}^4S_{3/2}$
Si VIII	$\lambda = 319.84$ Å	$2s2p^4\,{}^4P_{5/2} \to 2s^22p^3\,{}^4S_{3/2}$
Ni XVIII	$\lambda = 320.57$ Å	$3p^2P_{1/2} \to 3s^2S_{1/2}$
Fe XVII	$\lambda = 323.65$ Å	$2s^22p^53p^3P_2 \to 2s^22p^53s^3P_2$

X-ray spectroheliograph. In the figures, the areas for which the spectra were taken are marked: the active region NOAA 9742 (object no. 2) and the X3.4 flare (object no. 18) (see Table 1).

Choosing the Spectral Lines to Determine the DEM

Although more than 100 spectral lines are listed in the catalog of spectral lines in the range 280–330 Å (Beigman et al. 2005), most of them are blended and many have a low intensity. In addition, in accordance with the formulation of the problem of DEM determination, only the spectral lines whose contribution functions do not depend on the electron density should be used. Accordingly, we chose the following spectral lines: Ni XVIII 291.98 Å, Fe XXII 292.46 Å, Si IX 296.11 Å, Ca XVIII 302.19 Å, Si XI 303.33 Å, Fe XX 309.29 Å, Si VIII 319.84 Å, Ni XVIII 320.57 Å, and Fe XVII 323.65 Å (see Table 2). Except for the Si VIII–IX lines, the line contribution functions do not depend on the density.

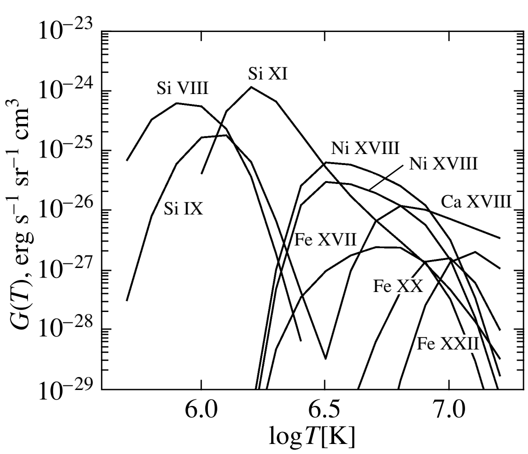

Fig. 3. Contribution functions of the spectral lines in the range 280–330 Å used to determine the DEM. These were calculated using CHIANTI 5.2.1 for $\log n_e = 9.0$ cm^{-3}, ionization equilibrium mazzotta_et_al.ioneq, and coronal abundances coronal_ext.abund.

The Si IX 296.11 Å line is blended with the Si IX 296.23 Å line and their contribution functions depend on the density. Our modeling of the plasma emission spectrum near 296 Å for various temperatures and densities that we performed by taking into account the spectroheliograph resolution showed that the Si IX 296.11 Å line contributes ∼75–80% of the intensity to the spectral region near 296.11 Å and that its contribution function changes by no more than 30% as the density changes in the range $\log n_e = 8.5$–11.

The contribution function of the Si VIII 319.83 Å line decreases approximately by half as the density increases from $\log n_e = 8$ to $\log n_e = 11$ cm^{-3}.

When calculating the DEM, we calculated the contribution functions for the density determined from simultaneous observations in the spectral range 176–207 Å (Shestov et al. 2009) if there were such measurements and for $\log n_e = 9.0$ otherwise.

The Si XI 303.33 Å line is located on the wing of the very intense He II 303.78 Å line and, in many cases, is unresolvable in the experimental spectrum. Therefore, the intensity of this line was taken as an upper limit and the accuracy was checked in the subsequent analysis.

The intensity of the Fe XXII 292.46 Å line is enough to be reliably determined only in flares. In other cases, its intensity was estimated as being below the level of measurement errors and was checked in the subsequent analysis.

The contribution functions of the chosen spectral lines calculated using the CHIANTI software are presented in Fig. 3. In this figure, the logarithm of temperature is along the x axis and the contribution functions $G(T)$ calculated for the density $\log n_e = 9.0$ cm^{-3} is along the y axis.

Spectral Line Intensities

To determine the intensities of the chosen spectral lines from experimental data, we used a technique similar to that used in Shestov et al. (2009) but adapted to the spectral range 280–330 Å. On the spectroheliogram, we subtracted the background and calculated a one-dimensional spectrum for the chosen region. The one-dimensional spectrum was obtained by summation over five vertical pixels in a direction perpendicular to the dispersion direction. In

Table 3. Intensities of the spectral lines used to determine the DEM

Object no. (Table 1)	Ni XVIII 291.98	Fe XXII 292.46	Si IX 296.11	Ca XVIII 302.19	Si XI 303.33	Fe XX 309.29	Si VIII 319.84	Ni XVIII 320.57	Fe XVII 323.65
1	90	28	39		1500		33	28	
2	915	50	418	275	3750	57	430	645	39
3	240	13	126	45	6950		138	123	
4	240	25	89	75	1170		134	129	
5	843	13	299	150	2500	50	465	415	
6	104	13	74	19	845		78	21	6
7	105	10	150	56	1540	13	128	63	10
8	13	3	139	16	1465		198	25	14
9	470	15	208	73	2108	23	161	138	18
10	575		259	36	1000	36	278	289	108
11	13		206		1000	13	310	14	10
12	133	13	46	50	698		50	45	
13	1568	180	235	1230	5000	148	160	825	118
14	2485	125	370	1318	5000	175	278	865	170
15	1030		250	285	4018	45	233	390	74
16	3135	215	554	2245	3540	303	595	1515	473
17	2130	405	648	2195	3000	218	805	613	258
18	3655	429	674	3203	3750	470	548	1820	416
19	1579	223	237	1555	1804	198	228	475	108
20	1540	150	210	445	2000	43	175	555	140
21	1615		179	1593	5000	185	88	678	135
22	3248	565	347	3215	3615	658	308	2198	704
23	2500		266	1640	3750	200	288	1325	315
24	2053		273	970	4075	230	291	1000	259
25	2173		177	2603	3500	375	350	1150	308
26	3015		219	1480	3634	198	545	1465	530
27	4750	908	753	4405	4250	978	423	2733	1165
28	3355		481	2080	5723	318	535	1635	540
29	3363	508	453	3950	3750	675	280	1730	588
30	3153		497	2085	5730	233	605	1788	540
31	2800	320	522	2110	3000	330	553	1445	383
32	3078	223	688	1800	3750	193	580	1455	485

Note. These were obtained from SPIRIT data in the range 280–330 Å. The intensity is given in digital counts. There is a blank in the table for the lines whose intensity could not be reliably determined from the experimental spectrum.

Table 4. Abundances used

Element	Abundance	Element	Abundance
H	12.00	S	7.27
He	10.90	Al	7.04
C	8.59	Ca	6.93
Mg	8.15	Ni	6.84
Si	8.10	Cr	6.21
Fe	8.10	K	5.67

Note. The abundances were taken from the CHIANTI software, sun_coronal_ext.abund.

the spectrum obtained, each line was fitted with a Gaussian:

$$i(\lambda) = A \exp\left[-\frac{1}{2}\left(\frac{\lambda - \lambda_0}{\sigma}\right)^2\right],$$

where $i(\lambda)$ is the intensity (in digital counts) of one pixel at wavelength λ, A is the peak line intensity (counts Å^{-1}), λ_0 is the central wavelength of the line, and σ is its width in Å. The total line intensity (in counts) was calculated using the formula $I = 2.5A\sigma_{\text{av}}$, where $\sigma_{\text{av}} = 0.1$ is the "average" width; it was taken for all lines. The accuracy of measuring the total intensities of individual lines is ∼10% for "strong lines" (like Ni XVIII 291.98 Å) and ∼30% for "weak ones" (like Fe XVII 323.65 Å).

The measured intensities for the chosen lines are listed in Table 3. The table gives the intensities in arbitrary units (digital counts), and the lines whose intensity should be considered as an upper limit are marked; when the intensity could not be reliably determined from the experimental spectrum, there is a blank. It should be noted that the spectroheliograms used differ in both exposure time and total sensitivity of the instrumentation related, for example, to degradation of the X-ray optics. Therefore, it makes sense to compare the relative line intensities only for the same observed object (the rows in Table 3). The line intensities for different observed objects can be compared only qualitatively.

DEM DETERMINATION

Formulation of the Problem

The emission power W_{ij} [erg s^{-1}] in a spectral line λ_{ij} for an optically thin plasma in volume V is defined by a volume integral of the form

$$W_{ij} = 4\pi \int G_{ij}(T(\mathbf{r}), N_e(\mathbf{r}))N_e^2(\mathbf{r})d\mathbf{r}, \quad (1)$$

where the functions $T(\mathbf{r})$ and $N_e(\mathbf{r})$ are, respectively, the plasma temperature and density at a given point of the plasma, $G_{ij}(T, N_e)$ [erg cm^3 s^{-1} sr^{-1}] is the contribution function related to the local plasma luminosity (emission power density) $F_{ij}(\mathbf{r})$ by the relation

$$G_{ij}(T(\mathbf{r}), N_e(\mathbf{r})) = \frac{1}{4\pi N_e^2(\mathbf{r})}F_{ij}(\mathbf{r}).$$

For the chosen spectral lines, except the Si VIII–IX lines, the coronal approximation holds at plasma densities $N_e < 10^{11}$ cm^{-3}. For such levels, G_{ij} does not depend on the density.

The integral over the volume V can be reduced to an integral over the temperature (Craig and Brown 1976; Urnov et al. 2007):

$$W_{ij} = 4\pi \int\limits_V G_{ij}(T)N_e^2 dV \quad (2)$$
$$= 4\pi \int\limits_{\Delta T} G_{ij}(T), y(T)dT,$$

where the integration is over the temperature range corresponding to the volume V. The function $y(T)$ [cm^{-3} K^{-1}], which is called the differential emission measure (DEM), characterizes the plasma distribution in temperature.

Note that the DEM is, in fact, the only quantity that contains information about the "amount" and temperature–density distribution of the emitting plasma, which can be extracted from the intensities of spectral lines. In addition, using it in interpreting the spectra can reveal the systematic errors of an instrumental nature (e.g., in the spectral sensitivity of the spectrograph) and in the abundances and atomic characteristics as well as the errors in the line identification or in the measured intensities caused by blending.

In this paper, we used version 5.2.1 of the CHIANTI software and database (Landi et al. 2006) to calculate the contribution functions and intensities of the spectral lines. The contribution functions were calculated by means of the gofnt.pro procedure. We used the coronal abundances sun_coronal_ext.abund (given in Table 4) and ionization equilibrium mazzotta_et_al.ioneq. To determine the density dependences of G_{ij}, we used the `pop_plot.pro` procedure. For the Si VIII–IX lines, $G(T)$ was calculated by taking into account n_e measured from simultaneous observations in the range 176–207 Å by of the SPIRIT spectroheliograph (see Shestov et al. 2009).

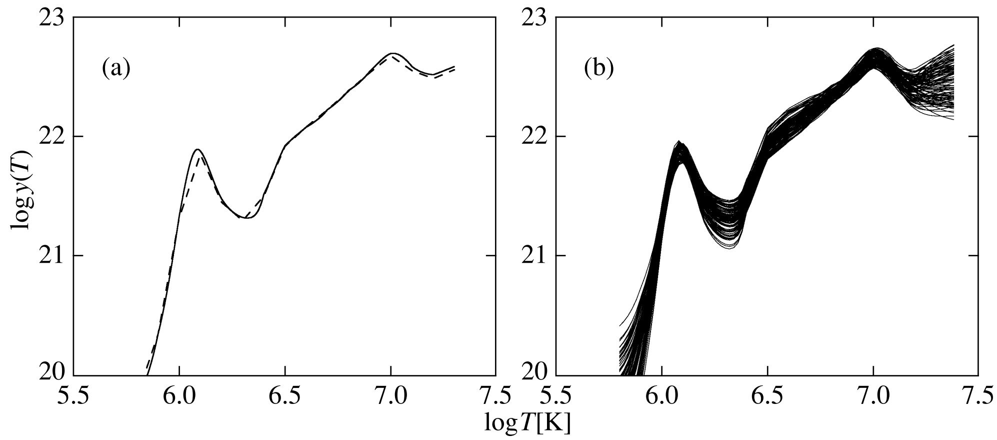

Fig. 4. Testing the iterative method of DEM determination: (a) the DEM obtained for the same input data with temperature steps of $\Delta \log T = 0.001$ (solid line) and $\Delta \log T = 0.1$ (dashed line); (b) the set of DEMs (100 tests) obtained for the same input data by introducing a random error of ±20%. In the panels, the logarithm of temperature is along the x axis and the logarithm of DEM in arbitrary units is along the y axis.

The Method of DEM Calculation

Various approaches are used to determine the DEM $y(T)$ from the intensities of spectral lines. These include the approaches based on the solution of a system of integral equations (Harrison and Thompson 1991), the forward-fitting method (Monsignori-Fossi and Landini 1991; Brosius et al. 1996), and others. To determine the DEM, we used an original probabilistic approach that has a number of advantages: in this approach, no regularization is required, and the solutions being obtained do not depend on the chosen temperature grid.

Let us introduce the functions

$$P(l) = \frac{W_l}{\sum\limits_l W_l}, \quad P(T) = \frac{4\pi y(T) \sum_l G_l(T)}{\sum\limits_l W_l}, \quad (3)$$

$$P(l/T) = \frac{G_l(T)}{\sum\limits_l G_l(T)},$$

that take on positive values and satisfy the normalization conditions

$$\sum_l P(l) = 1, \quad \int_{\Delta T} P(T)dT = 1,$$

$$\sum_l P(l/T) = 1.$$

Given (3), Eq. (2) can be rewritten as

$$P(l) = \int_{\Delta T} P(l/T)P(T)dT.$$

Here, $P(l)$ and $P(T)$ may be considered as the probability distribution functions of some random variables l and T, while $P(l/T)$ may be considered as the conditional probability distribution function of events (l/T). Let us apply the Bayesian theorem on conditional probabilities

$$P(T/l) = \frac{P(T)P(l/T)}{\sum\limits_T P(T)P(l/T)},$$

where $P(T/l)$ is the conditional probability distribution function of events (T/l). Multiplying both sides of the equation by $P(l)$ and summing over l yields

$$P(T) = P(T)\sum_l \frac{P(l)P(l/T)}{\sum_T P(T)P(l/T)} \quad (4)$$

$$= P(T)\sum_l \frac{P(l)P(l/T)}{P(l)}.$$

To construct an iterative scheme, let us represent the left- and right-hand sides of Eq. (4) as the $(n+1)$th and nth steps of the iterative scheme, respectively, and interpret $P(l)$ in the numerator as the experimentally measured quantities and in the denominator as those calculated on the basis of the nth iteration for $P(T)$. We will obtain the iterative scheme (the Bayesian iterative method (BIM); Urnov et al. 2007)

$$P^{n+1}(T) = P^n(T)\sum_l \frac{P^{\exp}(l)P(l/T)}{P^{\text{th}}(l)}. \quad (5)$$

A significant peculiarity of the method is that there is no "formal" requirement that the derived distributions $y(T)$ be smooth. In testing the method, we established that for a small number of iterations, $n = 5$–10, the solutions being obtained are smooth in form and very close to the DEM distribution obtained for the same spectral lines using the CHIANTI software in various experiments both qualitatively and quantitatively. When the number of iterations successively

Table 5. Ratios of the experimentally measured spectral line intensities to those calculated using the DEM

Object number (Table 1)	Ni XVIII 291.98	Fe XXII 292.46	Si IX 296.11	Ca XVIII 302.19	Si XI 303.33	Fe XX 309.29	Si VIII 319.84	Ni XVIII 320.57	Fe XVII 323.65
1	1.11	1.00	0.73		1.01		0.88	0.73	
2	0.88	1.21	1.31	0.86	0.99	1.68	0.88	1.32	0.76
3	0.98	1.22	1.10	0.95	1.00		0.96	1.06	
4	1.03	1.57	1.39	0.83	0.98		0.84	1.02	
5	0.97	1.35	1.64	0.90	0.98		0.66	1.13	
6	0.89	1.54	1.18	0.74	0.99		0.92	1.28	1.21
7	0.90	0.91	1.28	0.92	0.99	1.71	0.87	1.14	1.66
8	0.45	0.77	1.07	0.91	1.00		0.97	1.81	3.25
9	1.16	1.35	1.34	0.74	0.99	2.19	0.84	0.72	0.98
10	0.96		1.51	0.32	0.97	4.12	0.82	1.02	3.61
11	0.56		1.26		0.99	5.43	0.92	1.28	7.78
12	1.10	1.11	1.07	0.97	1.00		0.96	0.79	
13	0.95	0.82	1.09	1.04	1.00	1.10	0.86	1.06	1.13
14	1.07	0.69	1.28	1.05	0.99	1.22	0.85	0.79	1.17
15	1.04		1.11	1.03	1.00	1.60	0.93	0.84	1.38
16	0.94	0.70	1.32	1.03	0.99	1.20	0.87	0.96	2.01
17	1.09	0.90	1.32	1.04	0.98	0.91	0.88	0.67	1.80
18	0.95	0.78	1.57	1.02	0.98	1.26	0.77	1.01	1.51
19	1.11	0.74	1.31	1.06	0.99	1.14	0.86	0.71	1.04
20	1.08	1.67	1.31	0.80	0.99	0.83	0.86	0.83	1.83
21	0.96		1.01	1.24	1.01	1.15	0.69	0.86	1.10
22	0.82	0.93	1.41	0.93	0.99	1.53	0.79	1.17	2.51
23	0.90		1.08	1.15	1.00	1.21	0.96	1.01	1.64
24	0.94		1.05	0.99	1.00	1.97	0.97	0.97	1.82
25	0.87		0.80	1.20	1.01	1.33	1.06	0.98	1.55
26	0.91		0.81	1.06	1.02	1.32	1.05	0.94	2.38
27	0.86	1.03	1.63	0.89	0.98	1.59	0.68	1.06	2.81
28	0.91		1.12	1.10	1.00	1.43	0.94	0.94	2.09
29	0.90	0.71	1.56	1.02	0.99	1.40	0.73	0.99	2.03
30	0.86		1.17	1.14	1.00	1.13	0.93	1.04	2.11
31	1.01	0.87	1.33	0.98	0.99	1.29	0.86	0.85	1.94
32	0.95	0.91	1.43	1.00	0.98	0.99	0.80	0.95	2.23
Mean	0.94	1.04	1.24	0.96	0.99	1.36	0.87	1.00	1.76
σ	0.14	0.30	0.23	0.17	0.01	0.33	0.10	0.22	0.61

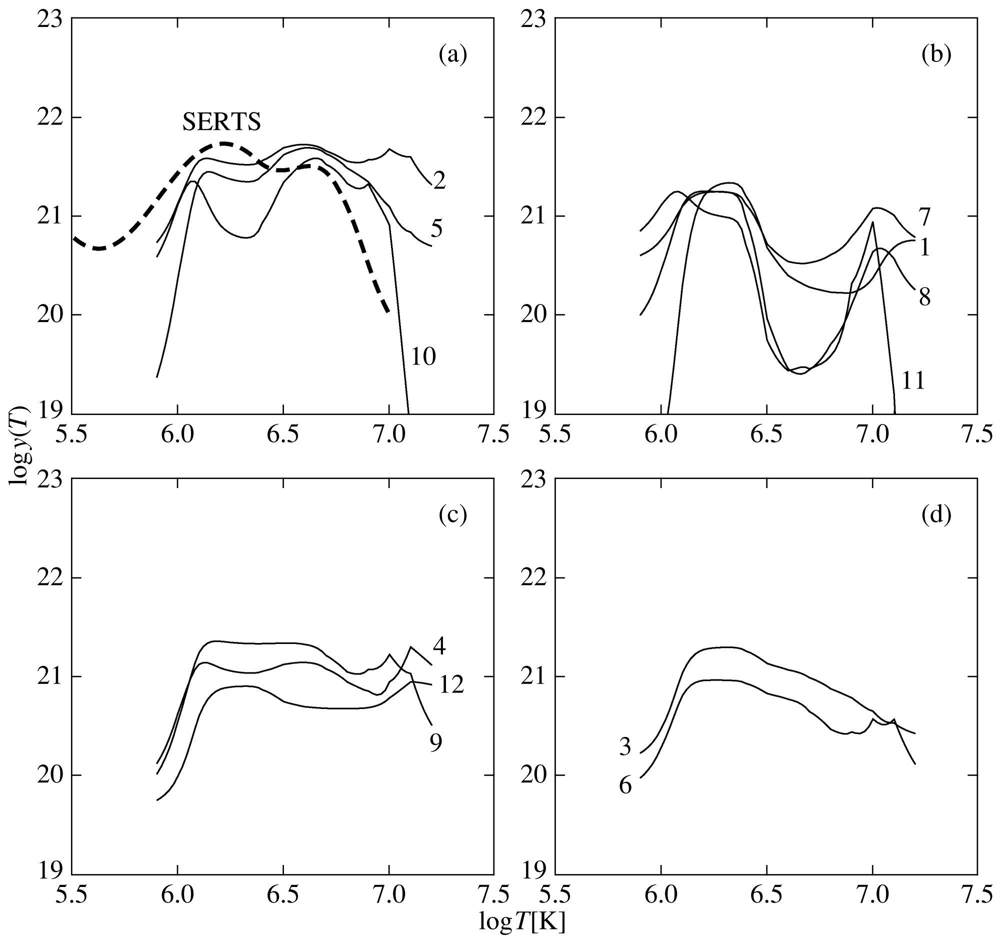

Fig. 5. DEMs of active regions from SPIRIT data. The logarithm of temperature is along the x axis, and the logarithm of DEM in arbitrary units is along the y axis. The derived DEMs were divided into four groups in accordance with their characteristic form. For comparison, the DEM for the active region observed in the SERT rocket experiment (dashed curve) is shown in panel (a). The curve number corresponds to the object number in Table 1.

increased, δ-like distributions $y(T)$ were observed for some sets of experimental lines. In particular, we used this fact to choose the number of iterations in our analysis of the DEM to obtain smoothed DEM curves used at this stage of investigation. These peculiarities and the confidence level of the derived DEMs will be analyzed in detail below.

Testing the Method

We performed a series of model tests to determine the sensitivity of the method to the temperature grid used, its sensitivity to errors in the line intensities, and possible constraints on the working temperature range.

Figure 4a compares the functions $y(T)$ obtained for the same input data with temperature steps of $\Delta \log T = 0.001$ (solid line) and $\Delta \log T = 0.1$ (dashed line).

We estimated the confidence level of the results obtained and the degree of stability of the method to the measurement errors of the line intensities by the following modeling. The initial set of spectral line intensities was varied by a random value as large as $\pm 20\%$ of the initial value and, subsequently, the DEM was calculated for the perturbed set of spectral line intensities. Figure 4b shows the DEMs obtained in this way for 100 tests, which demonstrate the confidence level. The picture did not change as the number of tests increased.

RESULTS OF DIAGNOSTICS

For the objects listed in Table 1, we determined the DEM temperature distributions. In our calculations, we used the temperature range $\log T = 5.9$–7.2, the step of the temperature grid was $\Delta \log T = 0.02$, and 10 iterations were in the iterative scheme. At such a number of iterations, the experiment/calculation ratio for most of the spectra and spectral lines has a mean value of ~ 1 and an rms deviation of $\sim 25\%$ (see Table 5).

Below, we present the results of our analysis of the DEMs for active regions and X- and M-class flares.

DEMs for Active Regions

The DEMs calculated for 12 active regions are shown in Fig. 5. We divided the derived distributions into four groups in accordance with their characteristic shape. In the figures, the logarithm of temperature is along the x axis, and the logarithm of DEM in arbitrary units is along the y axis. Near the curves, their numbers in accordance with Table 1 are given.

In Fig. 5a, each of the DEM distributions has two local maxima with temperatures $\log T = 6.2{-}6.1$ and $\log T = 6.5{-}6.7$. In the same figure, the DEM (dashed curve) calculated for an active region from SERTS experimental data (Brosius et al. 1996) is shown for comparison. The DEMs shown in Fig. 5b are characterized by a significant dip in the range $\log T = 6.5{-}6.7$ and a maximum near $\log T \sim 7.0$. The DEMs presented in Fig. 5c have an approximately constant value in the temperature range $\log T = 6.0{-}6.7$. The DEMs in Fig. 5d have a maximum near $\log T \sim 6.3$, following which the DEMs gradually decrease.

For most of the active-region spectra, the accuracy of determining the intensity of the Fe XXII 292.46 Å line is low due to its blending with the Ni XVIII 291.98 Å, Fe XV 292.28 Å, and Si IX 292.80 Å lines. To estimate the "sensitivity" of the derived DEMs to errors in the Fe XXII 292.46 Å line, we carried out a series of model experiments. The DEMs were calculated for the initial set of line intensities but with reduced Fe XXII line intensities. The reduction coefficients were chosen randomly within the range 0.1–1; 100 tests were performed for each observed object. The derived curves exhibited a spread in DEM at temperatures $\log T > 7.0$ reaching a tenfold difference. At lower temperatures, the DEMs did not change significantly (within the range marked in Fig. 4).

Analysis of the investigated active regions shows that 10 of the 12 objects contain a hot plasma in the temperature range $\log T = 6.8{-}7.2$ with an emission measure close in magnitude to that of a "cold" plasma and two active regions contain such a plasma in considerably smaller quantities.

A direct confirmation for the existence of a hot plasma is the solar image in the Mg XII $\lambda = 8.42$ Å resonance line shown in Fig. 2b for AR NOAA 9742 (object no. 2). This image was obtained by the Mg XII spectroheliograph that could record the emission only from a sufficiently hot plasma with a temperature above 5 MK, with the contribution function of the spectral line reaching its maximum at $T = 10$ MK. The bright sources in the Mg XII line correspond to the active regions that can also be seen in the EIT image and the spectroheliogram in the range 280–330 Å.

The results obtained lead to the conclusion about the existence of active regions with distinctly different temperature compositions; using 12 active regions as an example, we showed the existence of a hot plasma with $\log T = 6.5{-}7.0$ in active regions with a relatively large EM. The DEM determined for an active region in the SERTS rocket experiment (Brosius et al. 1996) qualitatively corresponds to the DEMs of several active regions observed by SPIRIT at temperatures $T < 5$ MK (see Fig. 5a).

DEMs for X-Class Flares

The DEMs calculated for X-class flares are presented in Fig. 6. Panel (a) shows the DEMs calculated for the spectra taken no later than 60 min after the flare maximum. These are objects nos. 18, 19, 22, 25, 27, 29, and 31 (see Table 1). Panel (b) shows the DEMs calculated for the spectra taken later than 60 min after the flare maximum. These are objects nos. 23, 24, 26, 28, 30, and 32. Spectra nos. 20 and 21 were also taken more than 60 min after the maximum, but the corresponding DEMs are shown in panel (c), because they differ in form from the first two groups.

All of the DEM distributions presented in panel (a), except the DEM for object no. 25 (marked by the dotted line), have a pronounced maximum at $\log T \approx 6.1$ and a minimum at $\log T = 6.2{-}6.4$ followed by a sharp rise in DEM with a maximum at $\log T = 7.0{-}7.1$.

The DEM distributions presented in panel (b), except object no. 32 (marked by the dotted line), have no maximum at $\log T = 6.1$, but they have a constant value at $\log T = 6.1{-}6.5$. The "hot" maxima of these distributions are observed at lower temperatures, $\lg T = 6.9{-}7.0$, and the curves have a sharper falloff at high temperatures than those presented in panel (a).

The DEMs shown in panel (c) differ qualitatively from those presented in panels (a) and (b) and more closely resemble the DEMs corresponding to active regions.

Given the time delay relative to the flare maximum, the above differences in DEM characteristics can be interpreted as the cooling of a hotter flare ($\log T \sim 7.0$) plasma and the heating of a colder plasma.

It is important to note that the local maximum in the DEM distributions at $\log T \sim 6.1$ observed near the flare maximum phase is close in magnitude to that in the DEM distributions observed in the SERTS (Schmelz et al. 1999), CDS (Landi and Landini 1998), and SUMER (Landi and Feldman 2008)

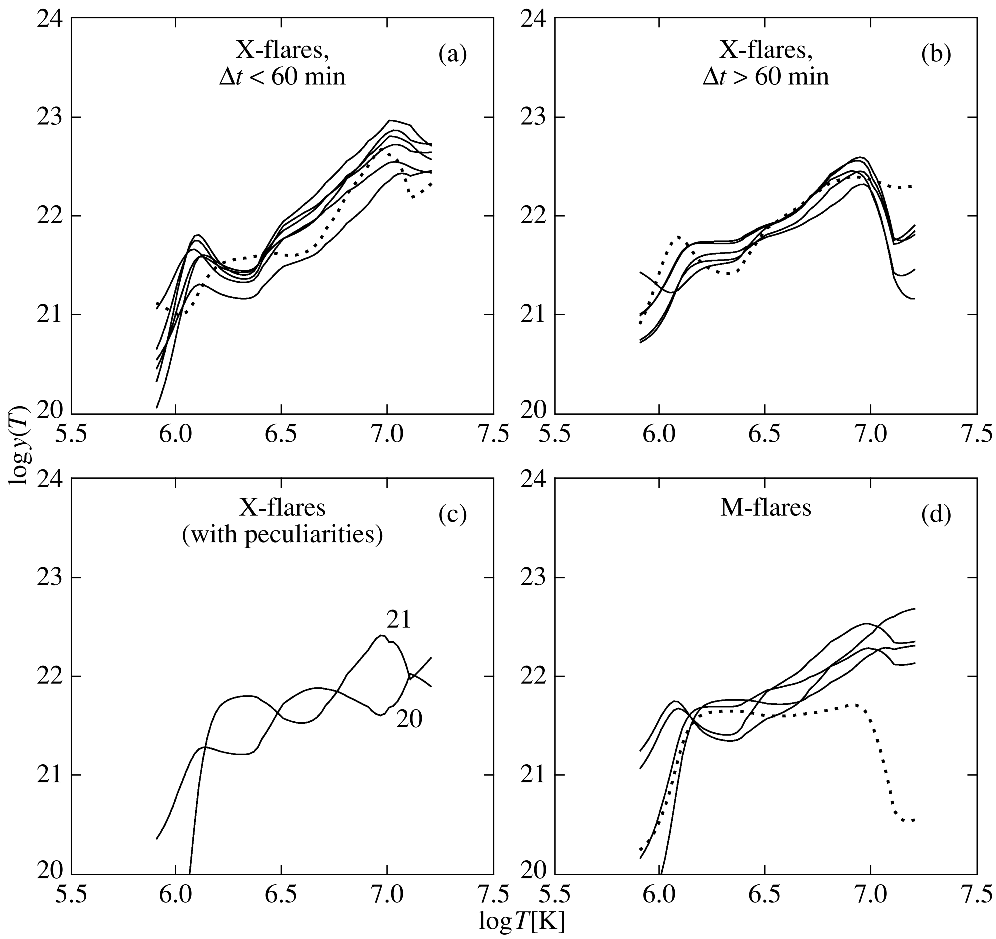

Fig. 6. DEMs for X- and M-class flares from SPIRIT data. The logarithm of temperature is along the x axis, and the logarithm of DEM in arbitrary units is along the y axis. The DEMs for X-class flares were divided into three groups in accordance with the time of observation after the flare maximum and the characteristic shape of the temperature dependence. See also the text.

experiments and a number of active regions considered here. This may suggest that stable plasma structures with a "characteristic" temperature $\log T \sim 6.1$, which are subsequently heated by the hotter plasma directly heated during the flare, exist in active regions.

Note also that a significant amount of "intermediate" plasma with temperatures $\log T = 6.5–7.0$ and the existence of a "limiting" temperature $\log T \approx 7.0$ are observed for all of the spectra considered. This is in good agreement with the data obtained for an M2 flare recorded by the spectroheliograph onboard the Skylab station (Dere and Cook 1979) and for flare events observed in the X-ray Mg XII 8.42 Å line (Urnov et al. 2007).

DEMs for M-Class Flares

The DEMs calculated for M-class flares are presented in Fig. 6d. The main features of the DEMs for M-class flares correspond to those for X-class flares: the maximum at $\log T = 6.1$ for some of the DEMs, the subsequent falloff, the framatic increase in DEM starting from $\log T = 6.5$, and the maximum at $\log T \sim 7.0$.

The DEM distribution for spectrum no. 15 (marked by the dotted line) taken more than 3 h after the flare maximum has a significantly lower value at $\log T \sim 6.5–7.0$.

No systematic differences (qualitative or quantitative) between the DEMs for X- and M-class flares were found, which may be indicative of common energy release and dissipation mechanisms in flares.

DEM Dynamics

Figure 7 presents the DEMs recorded at different flare decay phases. Panel (a) shows the DEM for an X17 flare observed on September 7, 2005. Spectra nos. 22, 23, and 24 were taken, respectively, 1 h, another 1.5 h, and another 1.5 h after the flare maximum. Panel (b) shows the DEMs for an X2.2 flare observed on September 10, 2005. Spectra nos. 29 and 30 were

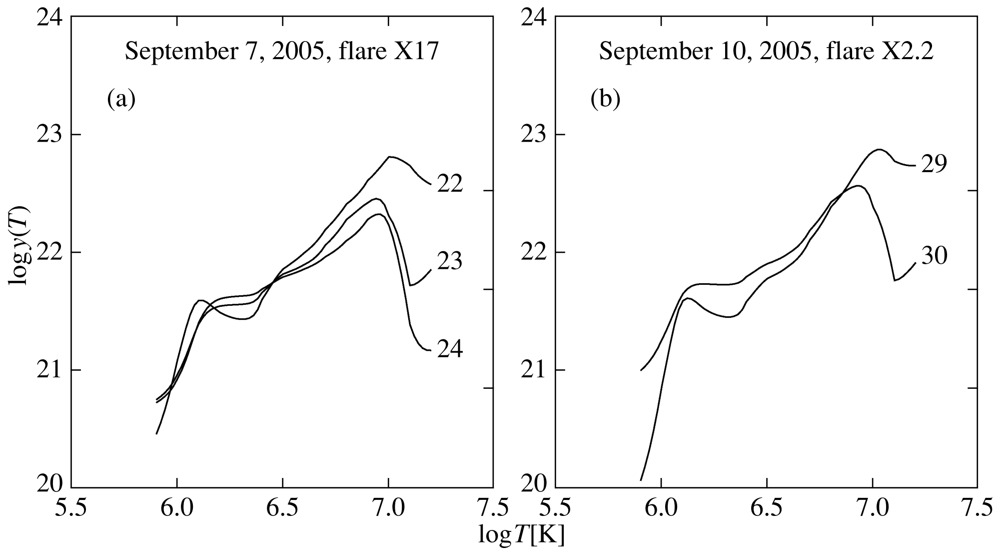

Fig. 7. Temporal DEM dynamics for two X-class flares from SPIRIT data. The logarithm of temperature is along the x axis, and the logarithm of DEM in arbitrary units is along the y axis.

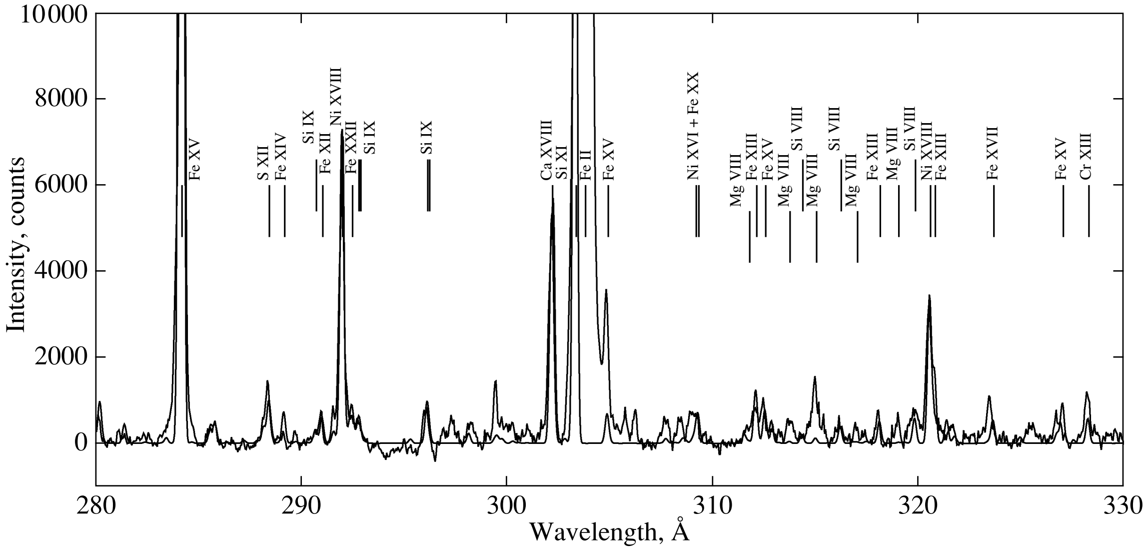

Fig. 8. Comparison of the experimentally measured and calculated (based on the DEM) spectra in the range 280–330 Å (object no. 21).

taken, respectively, ~12 min and another 1.5 h after the flare maximum.

The derived curves are consistent with our assumption about flare plasma thermalization.

Spectrum Modeling

Based on the calculated DEMs, we computed the coronal plasma emission spectra. The spectra were obtained using the CHIANTI software for the spectral range 280–330 Å; we used the ionization equilibrium mazzotta_et_al.ioneq, coronal abundances coronal_ext.abund, density $\log n_e = 9.0$ or the experimentally measured one. In addition, we took the parameters BINSIZE = 0.04 Å and FWHM = 0.2 Å. The measured and computed spectra for an X4.1 flare observed on the Sun on January 17, 2005, (object no. 21) are compared in Figs. 8 and 9.

A comparative analysis of the experimentally measured and computed spectra for various observed objects yielded the following results.

— In all of the spectra considered, the experimentally measured intensities of the Mg VIII (311.77, 313.74, 315.02, 317.03 Å) lines are considerably higher (up to a factor of 10) than their theoretical

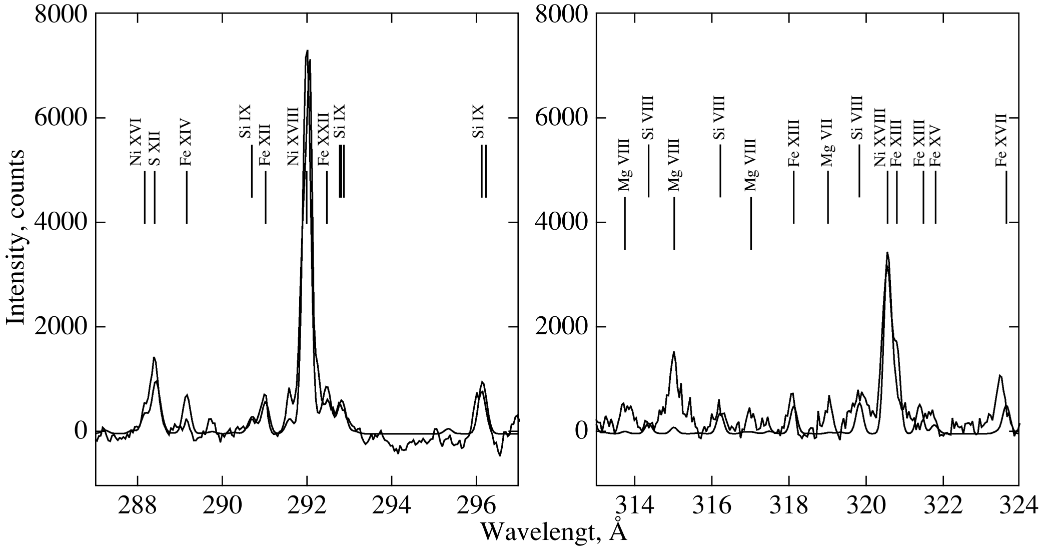

Fig. 9. Same as Fig. 8 but on an enlarged scale (object no. 21).

values. Since the "low-temperature" part of the measured DEMs depends mainly on the Si lines and, in addition, since the contribution functions of the Mg VIII and Si VIII lines have a similar temperature dependence, this difference can be explained by the use of improper abundances.

— The Fe XV 284.16, 304.89, 312.56, 321.77, and 327.03 Å spectral lines for all of the investigated spectra showed the following features: the experimental intensity is lower than the calculated one for the 284.16 Å line, higher than the calculated one for the 304.89 Å line, corresponds to the calculated value for the 312.56 Å line, higher than the calculated value for the 321.77 Å line, and lower than the calculated value for the 327.03 Å line. These discrepancies are observed for many of the spectra used here and can be explained neither by an abundance variation nor by a statistical error.

— The experimental intensity of the Cr XIII 328.27 Å line is higher than the calculated one for all of the spectra used here.

CONCLUSIONS

Our analysis of the DEM temperature distributions for flares and active regions leads us to the following conclusions.

(1) Four types of active regions with different temperature compositions characterized by peculiarities in the DEM distributions were observed.

(2) The presence of a hot plasma with a temperature $\log T = 6.8–7.2$ in active regions has been established for the first time.

(3) We have obtained the DEM distributions for intense long-decay solar flares for the first time and detected a similarity of the temperature compositions for flares of various classes at the decay phase.

(4) "Problem lines" were established in the spectral range 280–330 Å.

(5) Further studies of the confidence level of the derived DEM distributions, a more accurate and complete identification of the spectra of structures, and an increase in the volume of experimental data are needed to reach more detailed conclusions about the pattern of the temperature distributions in solar coronal structures.

ACKNOWLEDGMENTS

We are grateful to F.F. Goryaev and S.N. Oparin and S. Janucz from the Space Research Center, the Polish Academy of Sciences, for helpful remarks. This work was supported in part by the Russian Foundation for Basic Research (project nos. 08-02-01301-a and 08-02-13633-ofi_ts), the Basic Research Program of the Presidium of the Russian Academy of Sciences (Program no. 16, Part 3), the "Plasma Processes in the Solar System" and "Precision Optical Spectroscopy of Intraatomic and Intramolecular Transitions" Basic Research Programs of the Division of Physical Sciences of the Russian Academy of Sciences, and grant no. 218816 (the SOTERIA project, http://soteria-space.eu) of the Seventh Framework Program of the European Union (FP07/2007-2013).

REFERENCES

1. I. L. Beigman, S. A. Bozhenkov, I. A. Zhitnik, et al., Pis'ma Astron. Zh. **31**, 39 (2005) [Astron. Lett. **31**, 57 (2005)].
2. J. W. Brosius, J. M. Davila, R. J. Thomas, et al., Astrophys. J. Suppl. Ser. **106**, 143 (1996).
3. J. W. Brosius, R. J. Thomas, J. M. Davila, et al., Astrophys. J. **543**, 1016 (2000).
4. L. J. D. Craig and J. C. Brown, Astron. Astrophys. **49**, 239 (1976).
5. K. P. Dere, Astrophys. J. **221**, 1062 (1978).
6. K. P. Dere and J. W. Cook, Astrophys. J. **229**, 772 (1979).
7. R. A. Harrison and A. M. Thompson, SERC Techn. Report RAL-91-092 (1991).
8. E. Landi and U. Feldman, Astrophys. J. **672**, 674 (2008).
9. E. Landi and M. Landini, Astron. Astrophys. **340**, 265 (1998).
10. E. Landi, G. Del Zanna, P. R. Youngb et al., Astrophys. J. Suppl. Ser. **162**, 261 (2006).
11. B. C. Monsignori-Fossi and M. Landini, SERC Techn. Report RAL-91-092 (1991).
12. V. N. Oraevskii and I. I. Sobel'man, Pis'ma Astron. Zh. **28**, 457 (2002) [Astron. Lett. **28**, 401 (2002)].
13. J. T. Schmelz, J. Scott, and L. A. Rightmire, Astrophys. J. **684**, L115 (2008).
14. S. V. Shestov, S. A. Bozhenkov, I. A. Zhitnik, et al., Pis'ma Astron. Zh. **34**, 38 (2008) [Astron. Lett. **34**, 33 (2008)].
15. S. V. Shestov, A. M. Urnov, S. V. Kuzin, et al., Pis'ma Astron. Zh. **35**, 50 (2009) [Astron. Lett. **35**, 45 (2009)].
16. A. M. Urnov, S. V. Shestov, S. A. Bogachev, et al., Pis'ma Astron. Zh. **33**, 446 (2007) [Astron. Lett. **33**, 396 (2007)].
17. H. P. Warren and A. D. Warshall, Astrophys. J. **571**, 999 (2002).
18. I. A. Zhitnik, O. I. Bugaenko, J.-P. Delaboudiniere, et al., in *Solar Variability: From Core to Outer Frontiers,* Ed. by A. Wilson (ESA SP-506, Prague, 2002), p. 915.
19. I. A. Zhitnik, S. V. Kuzin, A. M. Urnov, et al., Astron. Vestn. **40**, 1 (2006).

Translated by V. Astakhov